Fundamental Efforts for Improving the Sensitivity of Magnetic Resonance Force Microscopy

by

Ye Tao

B.S. Biochemistry

Harvard University, 2009

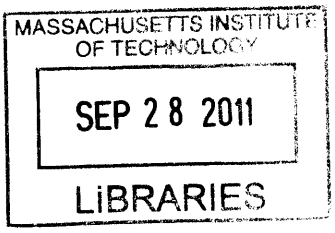

Submitted to the Department of Chemistry

in Partial Fulfillment of the Requirements for the degree of

MASTER OF SCIENCE

at the

Massachusetts Institute of Technology

July 2011

Signature of Author.....

Department of Chemistry

July 25th, 2011

Certified by.....

Professor Christian L. Degen

Thesis Supervisor

Accepted by.....

Professor Robert W. Field

Chairman, Departmental Committee on Graduate Students

Acknowledgements

I would like to thank Professor Christian Degen for welcoming me into his group to take part in its new and exciting research. I would also like to thank Dr. Gang Liu for the help he has given me at various stages of our efforts.

This work and its future continuations would not have been possible without the love and support of my wife, Qian, and of our parents. A sincere thanks to them all for supporting the various decisions I have made.

Contents

Chapter 1

Introduction

Complete understanding of the mechanisms of biological processes, indispensable for the rational design and testing of therapeutic strategies, can be greatly facilitated by easy and rapid access to macromolecular structures at the atomic resolution. As of 2011, a general method for rapid rendering of macromolecular and cellular structures with atomic resolution represents both a major challenge and a major need in science. Such a method would prove all the more valuable to understanding the conformational complexities of protein misfolding diseases and amyloid formation phenomena[1], caused by complex networks of structural transition reactions linking the monomeric, oligomeric, and polymorphic fibrillar forms of disease-causing proteins, the structures of which have only been rigorously characterized in a small number of cases [1–5].

To date, the majority of protein and RNA structures known have been solved by either X-ray crystallography or by NMR spectroscopy.[2] Many requirements on the sample prevent these methods from being generally applicable to biological specimens. First, since X-ray crystallography and NMR spectroscopy are techniques based on assessing the average properties of a macroscopic sample, a high degree of sample heterogeneity undermines their ability to solve structures [6]. Second, X-ray crystallography requires the sample protein to form ordered crystals. However, the procedure for crystallizing proteins remains a daunting trial-and-error process and important proteins like membrane

[1] Alzheimer's Disease, Parkinson's disease, Hungtington's disease, hereditary and transmissible forms of prion diseases, the prion phenomenon in yeast, and biofilm formation of bacteria

[2] See the Protein Data Bank for examples: www.rcsb.org/pdb/home/home.do.

proteins are impossible to crystallize in their native forms [7]. Recent advances in solid-state NMR (ssNMR) spectroscopy have made it possible to study membrane proteins, but the technique is still limited by protein size and by the need for order, at least at the local level [8]. For these reasons, the structural studies of macromolecule that contain high degrees of conformational heterogeneity and that are large in size have remained challenging, rare, and largely tackled, with difficulty, by computational approaches [9].

1.1 Principles of MRFM Operation

A genuine single-molecule technique, magnetic resonance force microscopy solves the issue of sample heterogeneity [10–13]. Even intrinsically disordered proteins like alpha-synuclein, linked to Parkinson disease [14], could be studied by individually imaging each molecule of the structural ensemble. With no need for signal averaging over separate copies of the molecule, as is the case in high-resolution cryo-EM, a continuum of conformational distributions can, in principle, be mapped out by MRFM.

Within the high static magnetic field and cryogenic environment of our MRFM setup, a μm-scale ultra-sensitive cantilever with sample attached at its tip is positioned close to a nanometer-sized magnetic tip and excited into mechanical resonance by applying a cyclically varying radio frequency (RF) pulse (e.g. $\omega(t) = \omega_0 + sin[\omega_c t]$) centered at the Larmor frequency (ω_0) of the sample nucleus (Figure 1.1). Frequency modulation of the RF is slow compared to the Larmor frequency, but matches the kHz-range frequency (ω_c) of the cantilever ($\omega_0 \gg \omega_c$). As a result of the slow change in RF frequency, the spins, in the rotating frame, adiabatically track the effective B field and undergo periodic inversions between the plus and minus directions of the Z axis. This periodic inversion of sample spins result in a periodic force between the nanomagnet and the cantilever, driving the latter to mechanical resonance, which is detected interferometrically as an increased displacement $\langle x^2 \rangle$ above the thermal background $\langle x^2 \rangle_0$. From conventional MRI, MRFM borrows the idea of selective sample nuclear excitation through the application of a high field gradient generated by a nanometer-scaled magnetic particle. Since the field strength now becomes a function of spatial position, only those spins in a resonant slice that have Larmor frequency matching with the applied RF frequency become excited. After collecting signal over a 3D grid, an image can be reconstructed by iterative means [13].

Figure 1.1: Left: Principles of MRFM [13] (see text for discussion). Right: Assembled MRFM Probe with 3D sample positioning system.

1.2 Unanswered Questions in Amyloid Diseases

Since the first suspicions half a century ago that prion and certain amyloid diseases replicate by a protein-only mechanism [15], much understanding of these protein-misfolding ailments has been gained, including *de novo*, *in vitro* generation of infections particles from native and recombinant proteins [16–18], their mechanisms of propagation by seeding and cross-seeding [19], linkage between certain genetic mutations and spontaneous disease generation [20], the mechanisms of fibril elongation and fragmentation [21–23], the presence of conformational polymorphism [23–25], the delicate interplay among fibril formation/fibril disaggregation with cellular chaperons such as Hsp104 [26,27], and even Darwinian evolution of prion conformational strains within host cell cultures [28]. Most work in this field has been based on biochemical analysis, cell work, and animal studies. Longer-range structural information from MRFM could contribute by facilitating the construction, from shorter-range ssNMR constraints, of structural models for different polymorphic forms of the amyloids. Rapid rendering of such models will accelerate understand of the relationship between strain conformation and physiological phenotype.

Despite the extent of literature on the subject, the identity of the toxic agent that directly causes neuronal degradation and cell death remains controversial. Mounting evidence is supporting the hypothesis that oligomeric intermediates, rather than mature amyloid fibrils, are the true culprit, and that amyloid fibril formation may actually be a last-resort protective mechanism of the cell for sequestering toxic intermediates [29–33]. The structure of non-fibrillar, oligomeric intermediates formed by Aβ1-40 and by the residues 106-126 of human prion protein have been shown by solid-state NMR spectroscopy to

contain cross-β structure nearly identical to those found in mature fibrils [34,35]. What is still not clear is the overall structure of oligomeric species, which can adopt different sizes and may have different physiological activities. The process of primary nucleation from oligomers to fibrils remains hazy. It is also a mystery why an antibody raised specifically against Aβ oligomers was found to be generally reactive against oligomers from a range of different peptides that share no primary sequence similarity [33]. Direct imaging of individual oligomers of different sizes and shapes by MRFM could help elucidating these mysteries. Detail of the application of MRFM to answers questions about amyloid will be described in a future PhD thesis.

In the rest of this thesis, I first describe our efforts toward the construction of a MRFM instrument with nanometer-resolution sample positioning, signal detection, and sub-Kelvin cryogenic capabilities. I then describe strategies we adopted for improving the resolution of MRFM from its current limit of 5 nm to 1 nm. These strategies include the fabrication of better magnetic field gradient sources and the fabrication of potentially better force sensors. I finally present experimental result of our fabrication efforts toward higher-gradient magnetic tips and diamond cantilevers.

Chapter 2

Construction of the MRFM Instrument

The MRFM is a complex instrument; laser light must be focused and stay focused onto a tiny custom mechanical cantilever a few micron wide; sample must be reliably attached to the tip of the cantilever, a custom nanometer-sized magnetic pillar must be position next to the cantilever with nanometer precision; efficient RF source must be present to manipulate the sample spins while avoiding the detrimental effect of thermal heating; and the whole setup need to be immersed within a millikelvin-temperature and ultra-high vacuum environment in order for the cantilever thermal noise and viscous damping effects to be sufficiently small.

Figure 2.1 shows a block diagram of our MRFM setup. This chapter describes the construction of the detection electronics consisting of a laser source, photodiodes connected to inverting operational amplifiers, the sample positioning system, and the dilution refrigerator.

2.1 Detection Electronics

In our MRFM system, the signal contained in the sensor cantilever motion is read out by optical interferometry. In order to enable readout of this signal, I constructed two 1550-nm infra-red lasers and two I-V converter/amplifer with gains of 10^5 and 10^7, respectively.

2.1.1 1550 nm Laser Box

Commercially available butterfly-style 12-pin 1550 nm laser diodes with built-in TEC were purchased. The + and - termini of the laser diodes were connected in parallel with protective Zener diodes with break-down voltages that would limit the maximum currents through the laser diode to within about 50% of the maximum allowable value of 200 mA. Connections to the TEC and the DC current supply were made through BNC connectors. The whole assembly was housed in a die-cast aluminum alloy Pomona box with dimensions 4.25in x 2.64in x 1.71in. Figure 2.2A shows the I-V characteristics of one of the resulting laser boxes. Figure 2.2B suggest that the protective zener diodes should have breakdown voltage below 3 volts in order for the maximum current passed through the laser diode to be below about 100mA. Figure 2.2C demonstrate that the protective diode wired in parallel with the laser diode has the desired property.

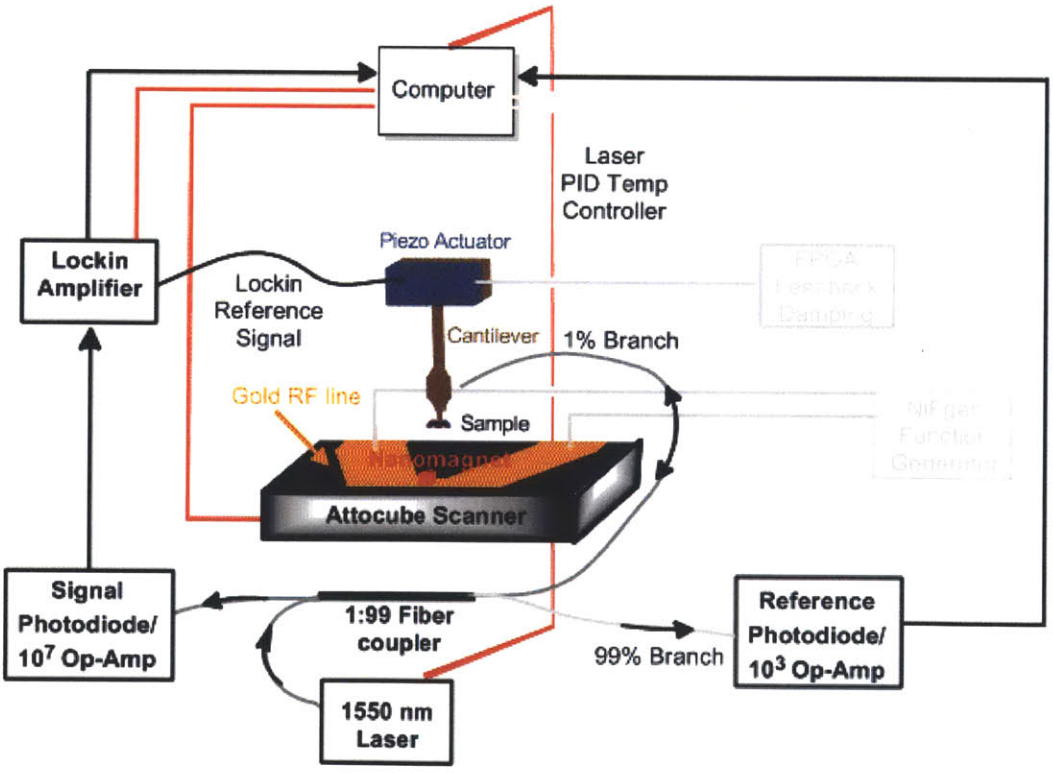

Figure 2.1: A block diagram of some key components of our MRFM system.

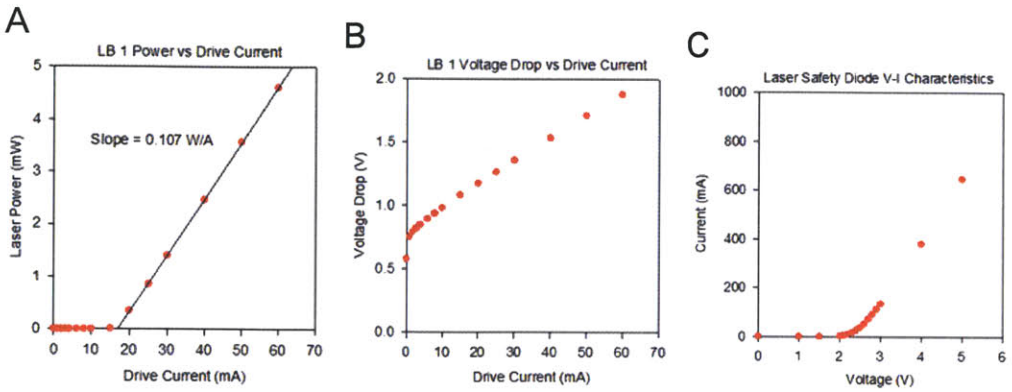

Figure 2.2: Calibration data for the 1550 nm laser. A: Output laser power vs the drive current. B: Voltage drop across a laser diode vs the drive current. V-I characteristics of Zener diodes connected in parallel with the laser diode for protection against excess current.

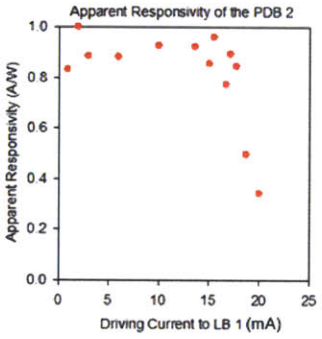

Figure 2.3: Responsivity of a photodiode-amplifier assembly with a gain of 10^5

2.1.2 I-V Converter and Amplifier

Photodiodes sensitive to IR light connected to either single-stage or two-stage inverting operational amplifiers were wired and housed inside the same type of Pomona boxes as for the laser boxes described above. With the resulting IR-sensitive photodetectors, I determined the linear response range of the photodiodes-amplifier assembly. Figure 2.3 together with Figure 2.2A suggest that the photodiode box 2, which has a I-V converter gain of 10^5, is linear only at very low laser illuminations in the microwatt range. This level of linear response range is sufficient for monitoring MRFM laser signal in the nanowatt range that are necessary for avoiding heating of the sample.

2.2 Sample Positioning System

Our setup employs a sample-on-cantilever geometry, with the nano magnetic pillar moving with respect to sample and cantilever during scanning. Figure 2.4 is a picture of our MRFM probe. 3D movement of the magnetic tip and RF line is achieved using Attocube positioning system shown in the upper portion of the picture.

To test the positioning system and the detection electronics, we performed a calibration experiment shown in Figure 2.5. A mirror was mounted on the Attocube positioning stage, perpendicular to the laser, and moved in directions approximately parallel (x) or orthogonal (y) to the laser beam. As the mirror moves through 1/2 of the wavelength, a full cycle of signal maximum to minimum is observed that result from the interference between the light reflected at the end of the fiber with the light that exits the fiber, reflects at the cantilever surface, and reenters the fiber.

Figure 2.6B and 2.6C show the resulting interference fringes as the mirror is moved with respect to the laser light in the y and x directions using the high-resolution x-y scanner, respectively. These interference fringes can be converted to linear displacement of the positioning system, taking into account the fact that each cycle of the fringe corre-

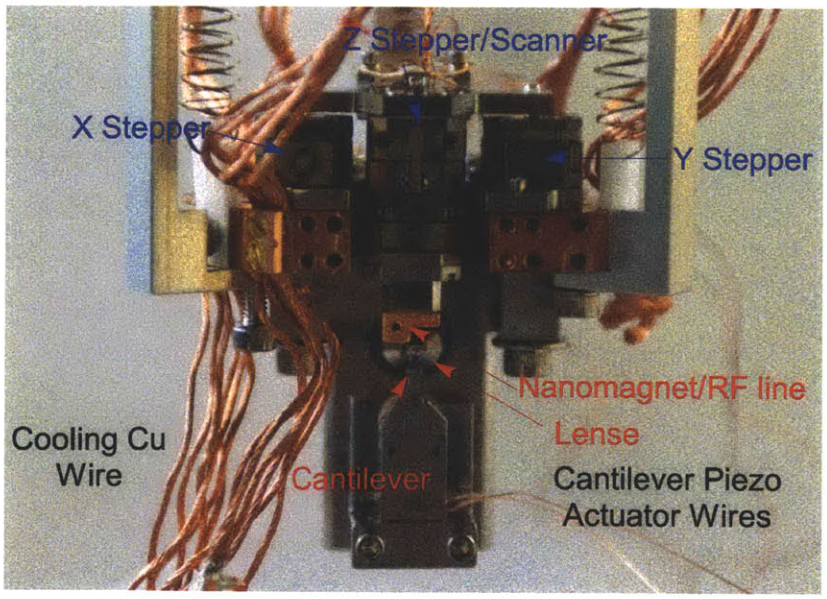

Figure 2.4: Our stability-improved MRFM probe.

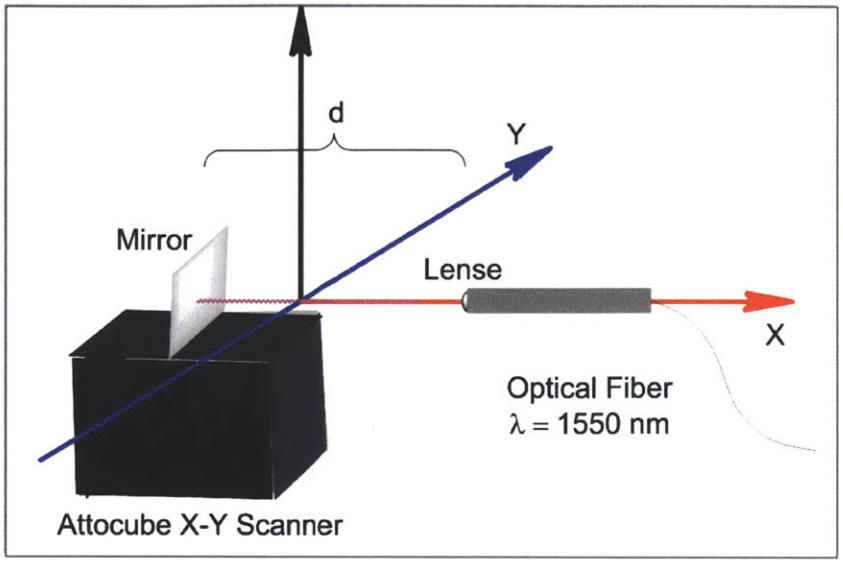

Figure 2.5: Experimental setup for the calibration of Attocube scanning system.

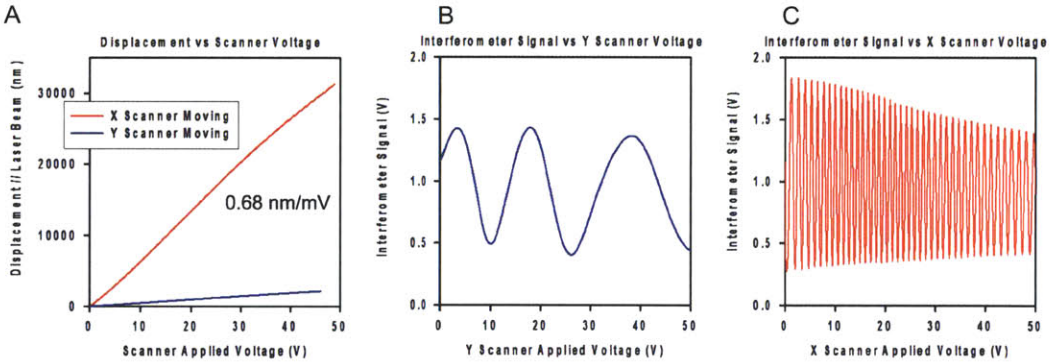

Figure 2.6: Calibration data of the x-y Attocube scanners. See text for discussion.

sponds to $\lambda/2$ in terms of actual spatial movement. The resulting displacements of the positioning system as a function of applied control voltages to the scanners are plotted in Figure 2.6A. The results suggest that the scanning blocks of the Attocube have good linear response to control voltage within a 20 μm by 20 μm scanning area at room temperature. Similar calibration at millikelvin temperatures will be carried out as a calibration of scanning spatial resolution when the system will be incorporated into our new dilution refrigerator.

Lastly, we demonstrated the capability of the system to act as a low-resolution AFM probe by scanning a piece of polished silicon wafer while reading out the amplitude of os-

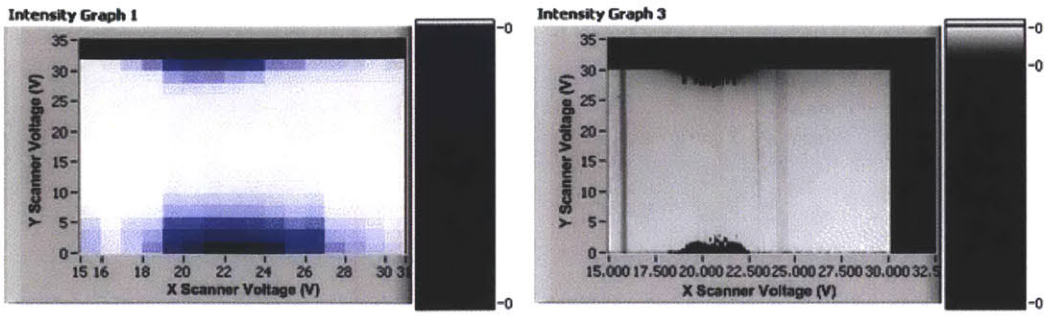

Figure 2.7: A piece of silicon wafer was scanned using our positioning system with a commercial AFM cantilever tip positioned perpendicular to the silicon surface. The cantilever was subjected to a constant driving voltage at fixed frequency. The amplitude of the cantilever oscillation is plotted in these figures.

cillation of a commercial AFM cantilever that is driven at constant frequency and voltage. Figure 2.7 shows the resulting image at 2 different scanning resolutions. The reproducibility of the features (very little given the flatness of silicon wafer), suggest that the sample positioning and signal acquisition systems are fully functional.

2.3 Dilution Refrigerator

A crucial component in sensitive MRFM detection is ultra-low temperature. This requirement is the result of the force sensitivity of the cantilever being limited by its thermal noise. In analogy to Johnson noise in resistors, the thermal noise in a MRFM measurement is related to the force power spectral density, S_F, of the cantilever.

$$S_F = 4\Gamma k_B T = \frac{4kk_B T}{\omega_c Q} \tag{2.1}$$

where k is the spring constant, ω_c is the vibrational frequency, and Q is the quality factor of the cantilever. The noise in a measurement with bandwidth $\Delta\nu$ is $\sqrt{S_F \Delta\nu}$.

To achieve a low temperature of tens of millikelvins, we purchased a dilution refrigerator from Leiden Cryogenics (Figure 2.8). This cryogen-free system is easy to operate and does not require the filling of liquid helium, allowing the desired experimental temperatures to be attained within a day with minimal labor.

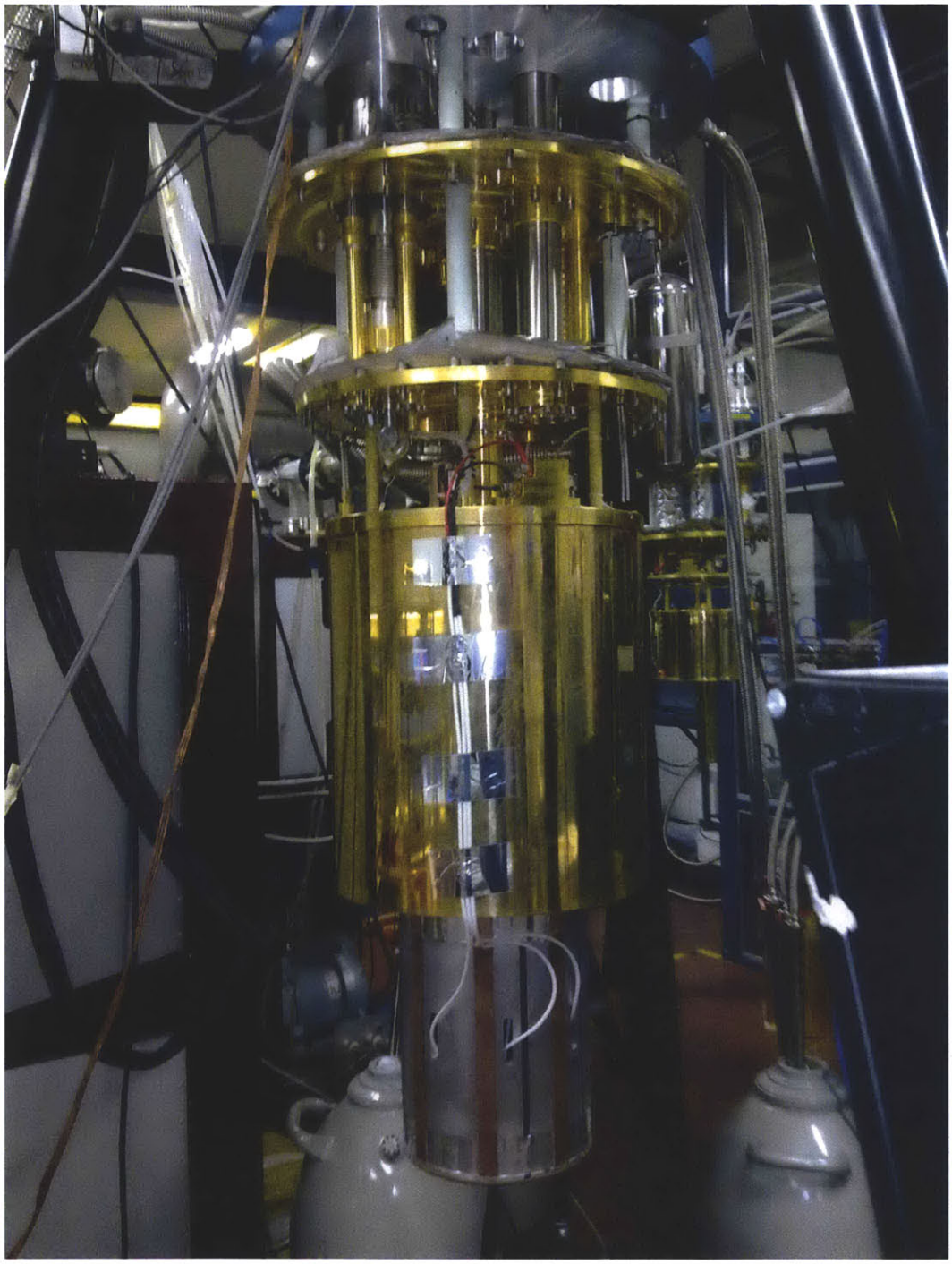

Figure 2.8: Dilution refrigerator used to cool our MRFM probe down to millikelvin temperatures.

Chapter 3

Fabrication of High-Magnetic Moment Fe/Co Nanopillars

3.1 Background

Both the spatial resolution and the signal-to-noise ratio (SNR, Equation (3.1)) of MRFM are highly dependent on the magnetic field gradient produced by the nanomagnet [12].

$$SNR = N\frac{(\mu_N \frac{\partial B_x}{\partial z})^2}{S_F \Delta f} \tag{3.1}$$

N is the number of spins with magnetic moment μ_N in the measurement volume, z measures the vertical distance between the nanomagnet top surface and the cantilever tip, and Δf is the measurement bandwidth. Magnetic tips produced by our current method of fabrication (Figure 3.1) have achieved maximum field gradients of 5×10^6 T m^{-1}, but is still significantly lower than the values of $3(1) \times 10^7$ T m^{-1} in existing pole tips used in drive heads that are less than 100 nm in lateral dimension [36]. Our first goal thus consists of fabricating stronger nanomagnets.

The current magnetic pillar fabrication strategy leads to at least four major defects. First, the resulting pillars are exposed to air and undergo steady oxidative degradation over time. Second, the geometry of the tips are ill-defined, because the hole on the evaporation mask gradually become clogged during the metal evaporation process, leading to tapered cones (Figure 3.1, Center). Third, the evaporated pillars do not stick well to the substrate,

Figure 3.1: Our previous method for fabricating nanomagnets (Developed by Ben Chui at Stanford). The method is based on evaporation of Fe and Co through small holes, defined by E-beam lithography, into a cavity underneath the mask. The magnets are exposed by N-methylpyrrolidone (NMP) liftoff.

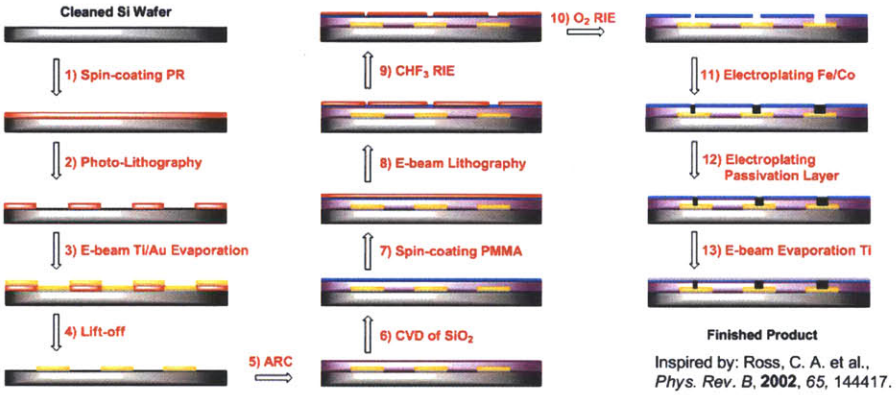

Figure 3.2: Current Strategy for Fabricating Next-Generation Magnetic Tips for Improved Force Sensitivity and Spatial Resolution.

and yield of the pillars is only around 50%. Fourth, the current pillars are pointy and stick out from the substrate surface. Such topologically sharp points may increase noncontact friction with the cantilever due to possible inhomogeneous charge accumulation.

3.2 Strategy

Given the inadequacy of the current method for producing optimal magnetic pillars, we propose the route in Figure 3.2 that aims to simultaneously solve all the mentioned defects of the previous-generation pillars. By electroplating Fe/Co into straight-walled cylindrical holes produced by reactive-ion etching, one is guaranteed good sticking of the resulting magnetic material and well-defined cylindrical shapes of the magnet [37]. Passivation of the magnetic pillars with a thin electroplated layer of aluminum (1-2nm) followed by an evaporated thin layer of titanium (1-2nm) would both retard oxidative degradation and produce a smoother surface that will be less prone to generating noncontact frictions

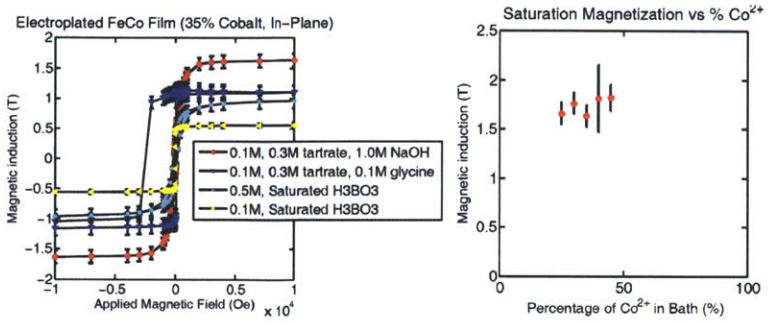

Figure 3.3: Vibrating sample magnetometer data showing the saturation magnetization of iron-cobalt thin films grown under different plating bath conditions.

with the cantilever[1]. Finally, as an additional benefit, electroplating into a cylindrical matrix has enable fabrication of metallic gold and silver cylinders thinner than 20 nm in diameter [38]. If similar results could be realized in our Fe/Co system, the proposed new nanopillar fabrication will likely play a decisive role in pushing the resolution of MRFM to new limits.

3.3 Results

We have initiated a study of the feasibility of producing high-quality Fe/Co alloy by electroplating. Initial screens of reported conditions in the literature [39, 40] has allowed the identification of a couple of promising electroplating conditions that produce films sufficiently smooth and with sufficiently high magnetic moment[2] to warrant the next step of investigation (Figure 3.3 and 3.4).

3.4 Outlook

The results demonstrate that electroplating is a viable method to produce high-quality magnetic material for making nano-pillars. Future experiments include the application of the optimal plating conditions to wafers that will have been pattern by e-beam lithography to contain cylindrical holes in a matrix of anti-reflective coating material (Steps 1-10 in Figure 3.2).

[1] See Section ?? for further discussion of noncontact friction.

[2] The maximum achievable magnetization for Fe/Co is about 2.4T.

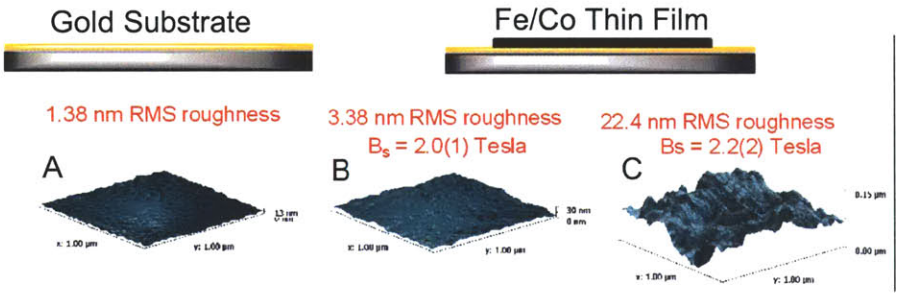

Figure 3.4: Preliminary Fe/Co electroplating results. A uniform layer of Fe/Co film were plated onto 4-inch silicon wafers coated with Ti/Au as conducting substrate. The smoothness of the gold substrate (A) and the resulting magnetic films under two plating conditions (B: [39]; C: [40]) were analyzed by atomic force microscopy and by vibrating sample magnetometry.

Chapter 4

Fabrication of Novel Cantilevers

4.1 Background

Going beyond state-of-the-art ultra-sensitive silicon cantilevers represents a challenge to the existing capability of top-down fabrication methods [12]. Alternative material and geometries have been proposed for future force sensors. Some are under active study, including carbon nanotubes [41], silicon nanowires grown by gold-catalyzed growth [42], and graphene [43]. One difficulty in embracing these techniques is that they often require specialized systems for detecting the motion of the force sensors, and that major undertaking and drastic change from our current probe design are needed. For example, to maintain laser focused on 50nm silicon nanowires during the cooling of the experimental apparatus, Nichol and Budakian constructed a dedicated piezo stage that correct for thermal drift of the nanowire sensor with respect to the laser [42]. Instead, we propose to investigate the feasibility of using single-crystal diamond as an alternative material to single-crystal silicon for fabricating sensitive cantilevers for force detection. Due to the regularity of the crystal lattice of diamond, mechanical structures based on it potentially would have low dissipation and high mechanical Q factor. It is hoped that single-crystal diamond cantilevers would out-perform silicon cantilevers in giving higher Q factor and, thus, lower thermal noise and higher sensitivity.

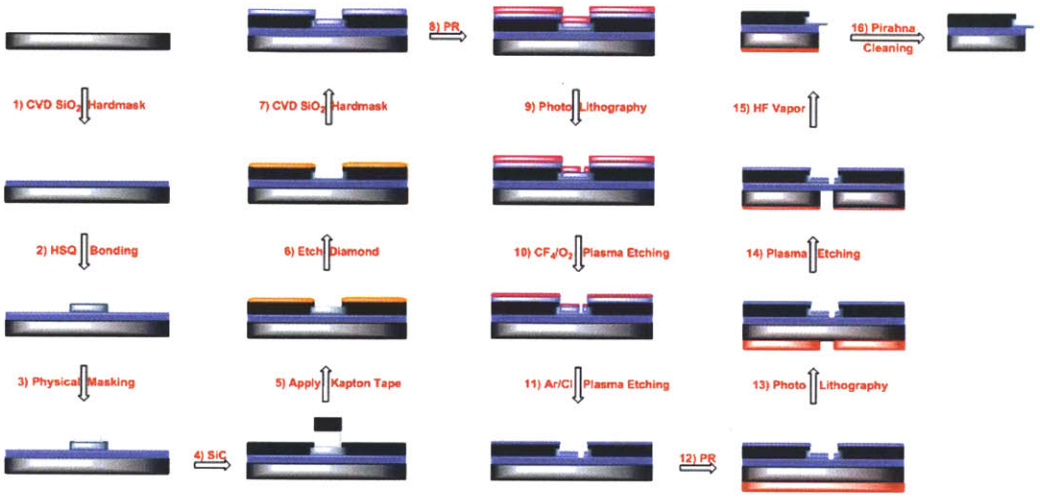

Figure 4.1: Proposed Fabrication of Single-Crystal Diamond Cantilever

4.2 Strategy

A proposed fabrication plan is presented in Figure 4.1. Major challenges in this plan include successful bonding of single-crystal diamond sheets to silicon carrier wafers, as well as smoothly etching the 10 μm-thick diamond sheet down to around 100nm, a thickness range optimal for ultra-sensitive force detection based on our experience with silicon precedents [44].

Another potential advantage of diamond cantilevers is the smaller dielectric constant of diamond compared to that of silicon, which might give smaller intrinsic noncontact friction and obviate the need to coat the cantilever with organic polymer prior to sample loading. If so, elegant UV-induced alkylation of H-terminated diamond surface would allow easy and specific targeting of samples such as amyloid oligomers to the tip of the cantilever.

4.3 Results

We tested the feasibility of fabricating micro-sized cantilevers from diamond by subjecting commercially available wafers carrying a 300 nm thin film of ultra-nanocrystalline diamond (UNCD) to the 10-step fabrication sequence after the diamond thinning step as showing in Figure 4.1. Optical images of the wafer at various steps of the fabrication pro-

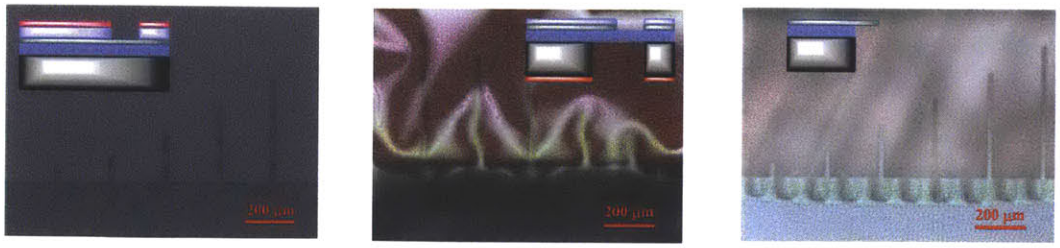

Figure 4.2: Images of UNCD wafers at various processing steps.

cess are shown in Figure 4.2. The yield of this idealized process was shown to be around 75%. A major loss mechanism is due to the stress of the silicon oxide layer, which sometimes spontaneously tear when underlying silicon wafer has been removed by backside reactive-ion etching (Figure 4.3).

4.4 Outlook

The success in the fabrication of nanocrystalline diamond cantilevers demonstrate that micron-sized MEMS devices can be carved out of diamond using conventional photolithography and etching techniques. The next challenge is to demonstrate that high-quality single-crystal diamond films can be fabricated by a top-down approach and also secured attached to a carrier substrate. To achieve these goals, I have followed and are currently improving upon the fabrication sequence shown in Figure 4.1.

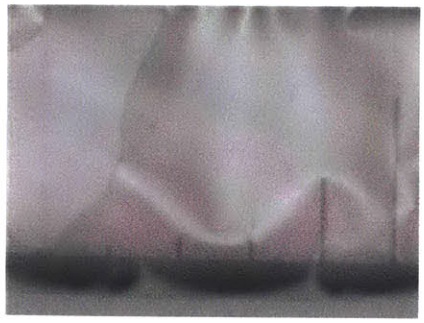

Figure 4.3: Images of UNCD wafers before HF release step. Thermal SiO2 layer has substantial strain and its tearing contributes to the loss of cantilevers.

Bibliography

[1] C. P. Jaroniec, C. E. MacPhee, V. S. Bajaj, M. T. McMahon, C. M. Dobson, and R. G. Griffin, "High-resolution molecular structure of a peptide in an amyloid fibril determined by magic angle spinning NMR spectroscopy," PNAS 101, 711-716 (2004)

[2] P. C. A. van der Wel, J. R. Lewandowski, and R. G. Griffin, "Solid-State NMR Study of Amyloid Nanocrystals and Fibrils Formed by the Peptide GNNQQNY from Yeast Prion Protein Sup35p," J. Am. Chem. Soc. 129, 5117-5130 (2007)

[3] C. Wasmer,A. Lange, V. Melckebeke, A. B. Siemer,R. Riek and B. H. Meier, "Amyloid Fibrils of the HET-s(218289) Prion Form a β Solenoid with a Triangular Hydrophobic Core," Science 319, 1523-1526 (2008)

[4] A. K. Paravastu, R. D. Leapmanb, W.-M. Yaua, and R. Tycko, "Molecular structural basis for polymorphism in Alzheimers β-amyloid fibrils," PNAS 105, 18349-18354 (2008)

[5] R. Tycko, "Solid-State NMR Studies of Amyloid Fibril Structure," Annu. Rev. Phys. Chem. 62, 279-299 (2011)

[6] R. L. Tuinstra, F. C. Peterson, S. Kutlesa, E. S. Elgin, M. A. Kron, and B. F. Volkman, "Interconversion between two unrelated protein folds in the lymphotactin native state," PNAS 105, 5057-5062 (2008)

[7] A. McPherson, "Introduction to protein crystallization," Methods 34, 254-265 (2004)

[8] H. Oschkinat, 2010 Winterschool NMR on Biomolecular Solid-State NMR, Stowe, Vt, Jan 24, (2004)

[9] C. K. Fisher, C. M. Stultz, "Constructing Ensembles for Intrinsically Disordered Proteins," Current Opinion in Structural Biology 21, 1-6 (2011)

[10] J. A. Sidles, J. L. Garbini, K. J. Bruland, D. Rugar, O. Züger, S. Hoen, and C. S. Yannoni, "Magnetic resonance force microscopy," Rev. Mod. Phys. 67, 249 (1995)

[11] A. Suter, "The Magnetic resonance force microscope," Progress in Nuclear Magnetic Resonance Spectroscopy 4, 239-274 (2004)

[12] M. Poggio and C. L. Degen, "Force-detected nuclear magnetic resonance: recent advances and future challenges," Nanotechnology 21, 342001 (2010)

[13] C. L. Degen, M. Poggio, H. J. Mamin, C. T. Rettnera, and D. Rugar, "Nanoscale magnetic resonance imaging" PNAS 106, 1313 (2009)

[14] M. G. Spillantini, M. L. Schmidt, V. M.-Y. Lee, J. Q. Trojanowski, R. Jakes, and M. Goedert, "α-Synuclein in Lewy bodies," Nature 388, 839-840 (1997)

[15] T. Alper, W. A. Cramp, D. A. Haig, and M. C. Clarke, "Does the agent of scrapie replicate without nucleic acid?" Nature 214, 764-766 (1967)

[16] J. Castilla, P. Saa, C. Hetz, and C. Soto, "In Vitro Generation of Infectious Scrapie Prions," Cell 121, 195-206 (2005)

[17] H. E. Sparrer, A. Santoso, F. C. Szoka Jr., J. S. Weissman, "Evidence for the Prion Hypothesis: Induction of the Yeast [PSI$^+$] Factor by in Vitro-Converted Sup35 Protein," Science 289, 595-599 (2000)

[18] F. Wang, X. Wang, C. G. Yuan, J. Y. Ma, "Generata a Prion with Bacterially Expressed Recombinant Prion Protein," Science 327, 1132-1135 (2010)

[19] C. J. Johnson, J. A. Pedersen, R. J. Chappell, D. MeKenzie, J. M. Aiken, "Oral Transmissibility of Prion Diseases Is Enhanced by Binding to Soil Particles," PLoS Pathogens 3, 0874-0881 (2007)

[20] E. Rogaeva, et al., "The neuronal sortilin-related receptor SORL1 is genetically associated with Alzheimer disease" Nature Genetics 39, 168-177 (2007)

[21] S. R. Collins, A. Douglass, R. D. Vale, J. S. Weissman, "Mechanism of Prion Propagation: Amyloid Growth Occurs by Monomer Addition" PLoS Biology 2, 1582-1590 (2004)

[22] T. P. J. Knowles, C. A. Waudby, G. L. Devlin, S. I. A. Cohen, A. Aguzzi, M. Vendruscolo, E. M. Terentjev, M. E. Welland, C. M. Dobson, "An Analytical Solution to the Kinetics of Breakable Filament Assembly," Science 326, 1533-1537, (2009)

[23] M. Tanaka, S. R. Collins, B. H. Toyama, and J. S. Weissman1, "The physical basis of how prion conformations determine strain phenotypes," Nature 442, 585-589, (2006)

[24] A. T. Petkova, R. D. Leapman, Z. H. Guo, W. M. Yau, M. P. Mattson, R. Tycko, "Self-Propagating, Molecular-Level Polymorphism in Alzheimer's β-Amyloid Fibrils" Science 307, 262-265 (2005)

[25] K. J. Verges, M. H. Smith, B. H. Toyama, and J. S. Weissman, "Strain conformation, primary structure and the propagation of the yeast prion [PSI^+]," Nature Structural and Molecular Biology 18, 493-499 (2011)

[26] S. DiSalvo, A. Derdowski, J. A. Pezza, and T. R. Serio, "Dominant prion mutants induce curing through pathways that promote chaperone-mediated disaggregation," Nature Structural and Molecular Biology 18, 486-492 (2011)

[27] J. Shorter, S. Lindquist, "Hsp104 Catalyzes Formation and Elimination of Self-Replicating Sup35 Prion Conformers," Science 304, 1793-1796 (2004)

[28] J. Li, S. Browning, S. P. Mahal, A. M. Oelschelegel, and C. Weissmann, "Darwinian Evolution of Prions in Cell Culture," Science 327, 869-872 (2009)

[29] C. A. McLean et al., "Soluble Pool of A-β Amyloid as a Determinant of Severity of Neurodegeneration in Alzheimer's Disease," Ann Neurol. 46, 860-866 (1999)

[30] J. Collinge, A. R. Clarke, "A General Model of Prion Strains and Their Pathogenicity," Science 318, 930-936 (2007)

[31] M. K. Sandberg, H. Al-Dojaily, B. Sharps, A. R. Clarke, and J. Collinge, "Prion propagation and toxicity *in vivo* occur in two distinct mechanistic phases," Nature 470, 540-542 (2011)

[32] M. Bucciantini, E. Giannoni, F. Chiti, F. Baroni, L. Formigli, J. Zurdo, N. Taddei, G. Ramponi, C. M. Dobson, M. Stefani, "Inherent toxicity of aggregates implies a common mechanism for protein misfolding diseases," Nature 416, 507-511 (2002)

[33] R. Kayed, E. Head, J. L. Thompson, T. M. Mcintire, S. C. Milton, C. W. Cotman, C. G. Glabe, "Common Structure of Soluble Amyloid Oligomers Implies Common Mechanism of Pathogenesis," Science 300, 486-489 (2003)

[34] S. Chimon, M. A. Shaibat, C. R. Jones, D. C. Calero, B. Aizezi, and Y. Ishii "Evidence of fibril-like b-sheet structures in a neurotoxic amyloid intermediate of Alzheimers b-amyloid," Nature Structural and Molecular Biology 14, 1157-1164 (2007)

[35] P. Walsh, P. Neudecker, and S. Sharpe, "Structural Properties and Dynamic Behavior of Nonfibrillar Oligomers Formed by PrP(106-126)," J. Am. Chem. Soc. 132, 7684-7695 (2010)

[36] Tsang C et al., "Head Challenges for Perpendicular Recording at High Areal Density," IEEE Trans. Magn. 42, 145 (2006)

[37] C. Ross et al., "Micromagnetic behavior of electrodeposited cylinder arrays," Phys. Rev. B 65, 144417 (2002)

[38] M. J. Burek and J. R. Greer, "Fabrication and Microstructure Control of Nanoscale Mechanical Testing Specimens via Electron Beam Lithography and Electroplating," Nano Lett. 10, 6976 (2010)

[39] S. K. Poznyak, V. V. Kharton, J. R. Frade, M. G. S. Ferreira, "Electroplating of iron films: Microstructural effects of alkaline baths," Materials Science Forum 514-516, p. 88-92, (2006)

[40] J. Chen, E. Flick, and H. H. Gatzen , "Minimizing oxygen inclusion when electroplating high saturation density CoFe for microelectromechanical system ," J. Appl. Phys. 107, 09A311 (2010)

[41] A. K. Huttel, G. A. Steele, B. Witkamp, M. Poot, L. P. Kouwenhoven, and H. S. J. van der Zant, "Carbon Nanotubes as Ultrahigh Quality Factor Mechanical Resonators," Nano Lett., 9, 2547-2552 (2009)

[42] J. M. Nichol, R. Budakian, E. R. Hemesath, and L. J. Lauhon, "Displacement detection of silicon nanowires by polarization-enhanced fiber-optic interferometry," Appl. Phys. Lett. 93, 193110 (2008)

[43] J. S. Bunch, A. M. van der Zande, S. S. Verbridge, I. W. Frank, D. M. Tanenbaum, J. M. Parpia, H. G. Craighead, and P. L. McEuen,, "Electromechanical Resonators from Graphene Sheets," Science 315, 490-493 (2007)

[44] T. D. Stowe, K. Yasumura, T. W. Kenny, D. Botkin, K. Wage, and D. Rugar, "Attonewton force detection using ultrasensitive silicon cantilevers," Appl. Phys. Lett. 71 , 288-290 (1997)